Laser Beam Welding analytical model when using wobble strategy

Authors: *I. Hernando, J.I. Arrizubieta, A. Lamikiz, E. Ukar.*

Affiliation: *Dept. of Mechanical Engineering, University of the Basque Country (UPV/EHU), Torres Quevedo 1, 48013 Bilbao, Spain.*

Highlights

- An analytical model for LBW that considers the wobble strategy is developed.
- Two-step model is presented, combining Carslaw-Jaeger´s and Rosenthal´s models.
- An error below 0.05 mm in widths and 0.3 mm in depth is obtained.
- Molten material movement is simulated using monopole, dipole and quadrupole models.
- The model predicts the SDAS with a 1 µm error.
- Surface cooling rate in the weld bead is calculated with an error below 10%.

Abstract

This article presents a model for estimating the thermal gradient, bead geometry and microstructure in the laser welding process, when the Wobble strategy is used. This method combines the main feed motion with a secondary high frequency orbital motion of the laser beam introduced by a galvanometer. The model is developed from an analytical approach and it is particularised to the case of the Wobble strategy through the implementation of two corrective factors. To this end, a two-step analytical model is presented. First, from Carslaw-Jaeger's theory, the thermal field of the upper face of the plates is modelled, allowing the width of the generated weld bead to be determined. The developed model includes the effect of the Wobble strategy as well as the initial transient regime. In a second step, the internal movement of the molten material within the melt-pool is modelled by means of the concepts of monopoles, dipoles and quadrupoles. Finally, the microstructure calculation is also implemented based on the previously estimated thermal gradient.

The model has been experimentally validated in Inconel 718 Nickel based alloy plates welding, using different process parameters and measuring the resulting bead section and microstructure. Errors below 0.05 mm and 0.3 mm are obtained regarding the bead width and depth, respectively, and differences below 10% are obtained between the estimated cooling rate by the model and experimental measurements. Finally, the estimated values of the Secondary Dendrite Arm Spacing parameters are below 1 µm of error in all tested cases.

Keywords: Laser beam welding, wobble, analytical, model, SDAS

1. Introduction

In areas of high level of excellence such as aeronautics, it is necessary to join components in a reliable way with minimum addition of weight. In fuselage parts, riveting has been the most frequent technique for joining components from initial aircraft designs with aluminium skin panels. Despite the addition of the extra-weight of the rivet to the structure, this is still in use because there is no microstructure change of the material. Besides, it offers the damping necessary to avoid stress concentrations when the fuselage is loaded and deformed during

flight. In other critical areas, such as motors, high quality welding is used to join different parts and reduce the weight of the entire structure. Mechanical properties of the melted area and heat-affected zone (HAZ) must be appropriate and this is only possible with technologies that provide homogeneous heating of the welding area. The electron beam welding (EBW) has been highly successful since the 70s. In this process, magnetic lenses guide accelerated free electrons towards the part in a vacuum chamber. When electrons impact on the surface, they generate non-elastic collisions allowing a fast and controlled beam penetration, and power densities up to 10^{12} W·cm^{-2} are reached [1]. Despite the high quality of EBW, its applications are limited because of the cost of the equipment and the complex electronic requirements to control the workpiece manipulator. Therefore, laser beam welding (LBW) has arisen as an alternative to this technology.

LBW was first developed in the 70s as one of the first applications of the laser technology for high quality welding. Nowadays power densities over 10^{9} W·cm^{-2} are possible resulting in small heat-affected zones in combination with high heating and cooling rates. With typical spot size between 0.2 and 13 mm and depth penetration proportional to the amount of power supplied, LBW is a versatile process capable of joining various materials in sectors like aeronautics [2]. Nevertheless, in critical applications, factors such as the extension of the HAZ and the uncertainty regarding the melt pool dynamics can vary the final properties of the joined region, so an accurate model of the welding process is convenient.

Industrial laser sources provide a known power density that can be controlled accurately, thus, the energy absorbed by the material, heat transfer by means of conduction and effects produced during heating and later cooling can be predicted using mathematics [3]. However, the simulation of welding processes is difficult due to the simultaneous appearance of thermal, mechanical and metallurgical phenomena [4].

The first analytical models were developed in the 1940s to study the thermal field in different part geometries irradiated by a heat source [5], [6], and Rosenthal developed a mathematical tool for understanding the heat flow generated by a moving heat source in welding [7]. Nevertheless, those models consider a steady state situation and conductivity and diffusivity were temperature independent. Simultaneously, Carslaw and Jaeger studied the heat transfer by conduction in metallic parts [8]. Nevertheless, no phase change or temperature dependent physical properties were considered.

In order to make a prediction as close as possible to reality, understanding phenomena such as plasma generation and melt-pool dynamics is essential [9]. Mazumder and Steen developed the first three-dimensional model considering a Gaussian heat source and solving heat transfer equations by finite difference numerical techniques. In their calculations, the keyhole formation period was negligible, and once created, it was considered as a blackbody because of absorptivity increase for the molten material. At same time, an energy loss coefficient was introduced to consider the heat losses by convection because of the shielding gas. The model was programmed using a quasi-static approach in order to simplify the mathematics.

Nevertheless, heating cycles must be accurately defined to model the mechanical behaviour of the welded areas [10] and this is still challenging nowadays [11]. The physics behind keyhole formation and its evolution into melt-pool dynamics is still under study [12]. Although experimental validation testing for LBW is difficult to perform, because of the simultaneous existence of plasma, liquid and solid material, appropriate numerical simulation can be helpful

in their understanding [13] specially in high-depth LBW modelling where there are still many aspects to be analysed [14].

That is, 80 years after the first pioneering research, the modelling of heat sources used for welding is immersed in a continuous improvement process. In addition to existing models, it is still necessary to study the feasibility of complex weld-like techniques with new models. For this reason, the aim of this work is to develop an analytical LBW model for nickel base alloys for aeronautic part application, that considers the movement of the molten material and temperature dependent properties.

Table 1: Used symbols and their physical description.

Symbol	Units	Description
(x,y,z)	[m]	Coordinates of the point where the temperature is obtained
(ξ,η,ζ)	[m]	Position of the laser beam centre
$Q''_{\zeta\zeta}$	[-]	Quadrupole coefficient in Z direction
$Q''_{\eta\eta}$	[-]	Quadrupole coefficient in Y direction
$Q''_{\xi\xi}$	[-]	Quadrupole coefficient in X direction
T_0	[K]	Temperature field at the beginning of the time step
t'	[s]	Initial time instant
$\Delta x, \Delta y$	[m]	Size of each element in the x and y axis, respectively
A	[-]	Absorptivity
d	[m]	Thickness of the plate
d_s	[m]	Diameter of the laser beam
d_w	[m]	Diameter of the wobble oscillation movement
$I(\xi,\eta)$	[W·m^{-2}]	Intensity function
k	[W·m^{-2} ·K^{-1}]	Thermal conductivity
L_{in}	[m]	Sum of the partial paths
P_{real}	[W]	Real power of the laser
P_{sim}	[W]	Power considered in the simulation
R	[m]	Distance between laser beam and studied point
S_{factor}	[-]	Area factor
S_h	[m^2]	Area inside the oscillating movement described by the laser beam
t_{factor}	[-]	Time factor
t_{in}	[s]	Time required for the laser spot to fill the circle described by the wobble movement
t_{step}	[s]	Time step
v_p	[m·s^{-1}]	peripheral speed of the laser beam
W	[K·W^{-1}]	Movement of the heat source on a semi-infinite part
α	[m^2·s]	Thermal diffusivity
T	[K]	Temperature field at the end of the time step
t	[s]	Time instant where the thermal field is calculated
v	[m·s^{-1}]	Feed rate

2. Model basis

2.1. Summary of the developed analytical model

A two-step model is presented for the Laser Beam Welding (LBW). First, based on Carslaw-Jaeger´s theory the thermal field on the upper face of the plates is modelled, what enables to determine the width of the generated weld bead. The developed model includes a new approach to the wobble strategy, where the transitory regime is considered. Then, in a second step, the internal movement of the molten material is modelled based on Rosenthal´s model, which enables to obtain the penetration of the weld bead.

2.2. Weld bead upper face modelling

The modelling of the heat transfer from the laser beam to the workpiece is based on the equations developed by Rosenthal [15]. However, a few modifications are introduced. On the one hand, the fact that in LBW the heat is distributed in an area is considered by means of the intensity function $I(\xi,\eta)$. On the other hand, the model developed by Carslaw and Jaeger that represent the heat transfer in a semi-infinite solid is considered [8]. Equation (1) defines the convolution multiplication of the A·I·W product, which defines the temperature rise at any point *(x,y,z)* of the part.

$$T(x,y,z) = \int_{-\infty}^{\infty}\int_{-\infty}^{\infty} A \cdot I(\xi,\eta) \cdot W(x-\xi, y-\eta, z-\zeta, v)\,dx\,dy \tag{1}$$

$$W = \frac{e^{\left[\frac{-v}{2\alpha}(x-\xi+R)\right]}}{2\pi k R} \tag{2}$$

$$R = \sqrt{(x-\xi)^2 + (y-\eta)^2 + (z-\zeta)^2} \tag{3}$$

The power-density absorbed by the substrate is defined by multiplying A and I, which enables to determine the intensity distribution in each time instant. The function *W* defined in equation (2) represents the movement of the heat source on a semi-infinite part. Equation (3) represents the distance from the laser beam centre *(ξ,η,ζ)* to the point where the temperature is being calculated *(x,y,z)*.

Nevertheless, before reaching a stable regime, in LBW the thermal field must go through a transitory regime. Therefore, the influence of time in the welding process must be considered in equation (1) in order to model the transient stage and equation (4) is achieved.

$$T(x,y,z,t) = \int_{-\infty}^{\infty}\int_{-\infty}^{\infty} AI(\xi,\eta)W(x-\xi, y-\eta, z-\zeta)U(R,t,v)\,dx\,dy \tag{4}$$

$$U(R,t,v) = \frac{R}{\sqrt{\pi}}\int_{1/\sqrt{\alpha t}}^{\infty} e^{\frac{-(R\tau^2-\frac{v}{\alpha})^2}{4\tau^2}}d\tau = \frac{1}{2}\left[1 - \operatorname{erf}\left(\frac{R-vt}{2\sqrt{\alpha t}}\right) + e^{Rv/\alpha}\left(1 - \operatorname{erf}\left(\frac{R+vt}{2\sqrt{\alpha t}}\right)\right)\right] \tag{5}$$

$$\tau = [\alpha(t-t')]^{-1/2} \tag{6}$$

The *erf* error function is defined for a general variable *a* according to equation (7).

$$\operatorname{erf}(a) = \frac{1}{\sqrt{\pi}}\int_{-a}^{a} e^{-t^2}dt = \frac{2}{\sqrt{\pi}}\int_{0}^{a} e^{-t^2}dt \tag{7}$$

This way, the time-dependent equation that determines the temperature field is obtained. However, if temperature rise is to be calculated in the regions close to where the laser beam

strikes, the parameter *R* tends to zero and introduces a singularity in the parameter *W*. In order to solve this issue, in the cases where the *R* parameter value is below the unit, instead of using the parameter *W*, the following $W_0 = lim_{z\to 0}\, W$ parameter is used.

$$W_0 = \frac{e^{\frac{-(vz)^2}{2\alpha}}}{2\pi k \Delta x \Delta y}\left[\Delta x \ln\left(\frac{w_1 + \Delta x}{w_1 - \Delta x}\right) + \Delta y \ln\left(\frac{w_2 + \Delta y}{w_2 - \Delta y}\right) - 4z\left(\arctan\left(\frac{w_1}{2z}\right) + \arctan\left(\frac{w_2}{2z}\right)\right) + 2z\pi\right] \quad (8)$$

$$w_1 = \sqrt{\left(\frac{\Delta x^2 + 4z^2\cos^2\beta}{\sin^2\beta}\right)}$$

$$w_2 = \sqrt{\left(\frac{\Delta y^2 + 4z^2\sin^2\beta}{\cos^2\beta}\right)} \quad (9)$$

$$\beta = \arctan\frac{\Delta y}{\Delta x}$$

2.3. Fourier Transform

One of the main drawbacks of the analytical methods is the complexity to solve the obtained equations. Double integrates can be solved by means of various methods, such as the multiple integration method. However, those methods are slow compared to the Fourier Transform (FT). Consequently, in order to ensure a low computational cost and a high speed of the model, the FT method is used. For this purpose, the FFT2 module of Matlab R2018b is employed.

Besides, thanks to the usage of the convolution multiplication, the model solves directly the double integral defined for the temperature field calculation for each z-level surface. Therefore, the model obtains the temperature field of all nodes in each height constant surface, and each surface is calculated independently.

The calculated FT of the intensity, *F(I),* varies as the heat source moves and therefore, the model includes the effect of a moving heat source. Similar to the intensity, the Fourier transformation of *W* and *U* multiplication is calculated, *F(W·U)*. Afterward, the Fourier transform of the bi-dimensional temperature field is obtained by means of equation (10).

$$F(T) = F(W \cdot U) * F(I) \quad (10)$$

In order to calculate the temperature increase in each point of the heated part the reverse FT is employed, equation (11), where the absorptivity, *A*, and area of the employed mesh are included, $dS = \Delta x \cdot \Delta y$ and the temperature field at the beginning of the time step, T_0, is considered.

$$T(x, y, z, t) = A \cdot F^{-1}\big(F(T)\big) \cdot dS + T_0 \quad (11)$$

2.4. Wobble strategy

The coupling of fast optics in the laser welding head offers the capability to obtain different weld sizes using a small laser spot, which increases the flexibility of the employed laser equipment. Wobble strategy combines two movements, as it is detailed in Figure 1, the main feed rate, a linear movement, and a circular superposed oscillation movement of the laser beam, which is around 50 times faster.

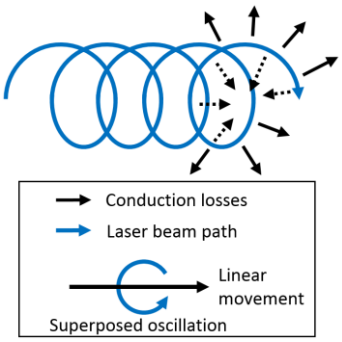

Figure 1: Wobble strategy scheme, where linear and oscillation movements are combined.

Modelling the wobble strategy is a complex task and classical theories provide no possibility to include the oscillation movement of the laser beam when a wobble strategy is used. Besides, considering the heat transfer in every single location of the laser beam as it moves implies an excessive cost.

$$P_{sim} = \frac{P_{real} \cdot S_{factor}}{t_{factor}} \tag{12}$$

Because of the employed simplifications, two factors have been included in the model to ensure the correspondence between the model and the experimental results, see equation (12). These parameters are applied over the value of the P_{real} in order to obtain the P_{sim}.

2.4.1. Area factor

Based on the assumption that the oscillation velocity of the spot is much higher than the feed rate, it is considered that the laser beam has an annular shape and the whole ring is heated simultaneously. Nevertheless, the equations of the analytical model can only solve the thermal field in the case of a circular heat source, see Figure 2, and consequently, an area-factor is included, equation (13).

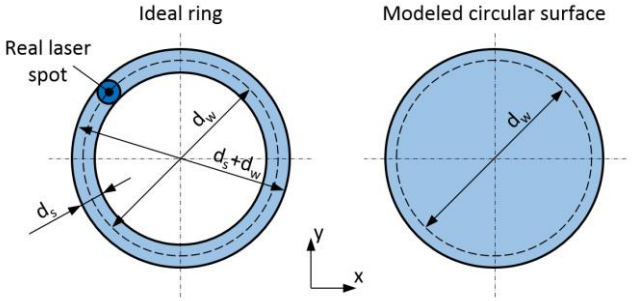

Figure 2: Approximation of the heat source.

$$S_{factor} = \frac{S_{sim}}{S_{ideal}} \tag{13}$$

$$S_{sim} = \frac{\pi(d_w + d_s)^2}{4} \tag{14}$$

$$S_{ideal} = \frac{\pi(d_w + d_s)^2}{4} - \frac{\pi(d_w - d_s)^2}{4} = \pi d_w d_s \tag{15}$$

A time step that ensures a minimum overlap of the successive loops swept by the laser is considered in the analytical model. Therefore, the value of the employed time step depends on the process parameters.

$$t_{step} = \frac{d_s}{v} \tag{16}$$

2.4.2. Time factor

In the real situation where the laser beam describes an oscillating movement, there is an area in the centre of the ring where no heat is introduced. Nevertheless, in the proposed assumption of using a circular heat source, the laser power that irradiates the surface of the substrate needs to be corrected according to a time factor.

The time factor, t_{factor}, is adjusted to an empirical equation, based on results of experimental test. The aim is to develop an equation that is valid for different welding conditions and considers the influence of the most relevant parameters when a wobble strategy is used. For this purpose, besides the laser feed rate and the wobble parameters, the time required for the laser spot to fill the circle described by the wobble movement (t_{in}), the sum of the partial paths (L_{in}) and the peripheral speed of the laser beam are considered (v_p). Similarly, in order to consider the effect of the heat transfer towards the centre of the described circle in the wobble strategy, the area inside the circle is calculated, which is named as S_h.

$$L_{in} = d_w \cdot \sum_{n=1}^{\frac{d_w+d_s}{d_s}-1} arctan\left(\sqrt{\left(\frac{d_w}{n \cdot d_s}\right)^2 - 1}\right) \tag{17}$$

$$t_{in} = L_{in}/v_p \tag{18}$$

$$S_h = \frac{\pi}{4} \cdot (d_w - d_s)^2 \tag{19}$$

2.5. Weld bead penetration modelling

Despite the modifications introduced to Carslaw-Jaeger´s theory, it is not capable of modelling the movement of the molten material within the melt pool. For this purpose and based on the multipole theory, the equations published by Nunes are considered, where the internal movement of the molten material is considered [16]. First, the heat source is represented as repetitive punctual monopoles distributed among the part, see the black dots in Figure 3. In order to determine the influence of the heat in a surface situated at *z* depth, *2·P* power heat sources separated by a *2·d* distance must be considered, where *d* is the thickness of the plate.

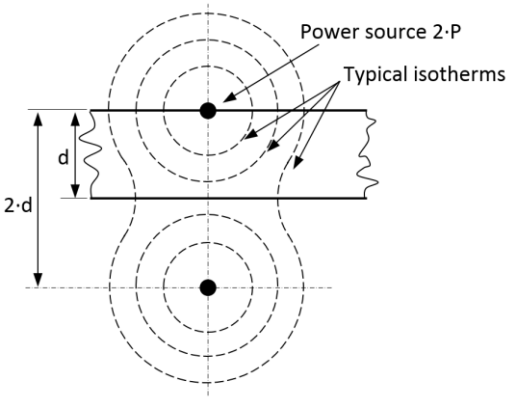

Figure 3: Monopole model representation.

Being *V* one of the solutions of the heat transfer equations and *(ξ,η,ζ)* the position of the heat source, Rosenthal defined the monopole model by means of equations (20-25).

$$\frac{\partial^2 T}{\partial x^2} + \frac{\partial^2 T}{\partial y^2} + \frac{\partial^2 T}{\partial z^2} = -\frac{v}{\alpha}\frac{\partial T}{\partial x} \tag{20}$$

$$V = \frac{1}{4\pi k}\frac{e^{-\frac{v}{2\alpha}(R+x-\xi)}}{R} \tag{21}$$

$$T - T_0 = 2P\left[V(R_0) + \sum_{n=1}^{\infty}\left(V(R_n) + V(R_{n'})\right)\right] \tag{22}$$

$$R_0 = \sqrt{x^2 + y^2 + z^2} \tag{23}$$

$$R_n = \sqrt{x^2 + y^2 + (z - nd)^2} \tag{24}$$

$$R_{n'} = \sqrt{x^2 + y^2 + (z + nd)^2} \tag{25}$$

Afterward, Nunes represented geometrically the phase change in a moving melt pool by means of dipoles. As the melt pool advances together with the laser beam, the material on the front is melted, whereas material on the backside is solidified. Therefore, the heat source can be represented by means of opposed dipoles. The distance between the poles is *Δξ,* see Figure 4, generating an opposed set between the two poles.

$$T - T_0 = \oint_{S'} \rho L v V(\xi, \eta, \zeta) d\eta d\zeta \tag{26}$$

$$T - T_0 \approx 2P\Delta\xi\left[\frac{V\left(\frac{\Delta\xi}{2}\right) - V\left(\frac{\Delta\xi}{2}\right)}{\Delta\xi}\right] \tag{27}$$

When $\Delta\xi$ tends to zero:

$$T - T_0 \approx \mathcal{Q}'_{\xi}\left(\frac{\partial V}{\partial \xi}\right)_0 = \mathcal{Q}'_{\xi} \cdot V_0 \cdot \left[\left(1 + \frac{x}{R}\right)\frac{v}{2\alpha} + \frac{x}{R^2}\right] \tag{28}$$

$$\mathcal{Q}'_{\xi} = \lim_{\Delta\xi \to 0} 2P\Delta\xi \tag{29}$$

$$V_0 = \frac{1}{4\pi k}\frac{e^{-\frac{v}{2\alpha}(R+x)}}{R} \tag{30}$$

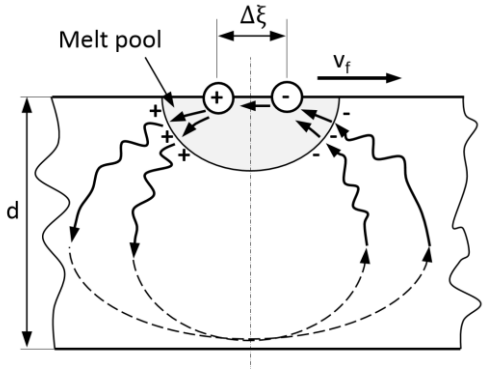

Figure 4: Dipole representation of phase change.

Once the influence of monopoles and dipoles is included in the developed model, the influence of quadrupoles needs to be considered in order to simulate the molten material movement, see Figure 5. The movement of the molten material inside the melt pool is mainly due to the surface tension and is directly influenced by the sulphur concentration and the process parameters [17]. Molten material moves from higher-pressure regions to lower-pressure regions. Consequently,

instead of accumulating heat in the centre of the melt pool, heat is transferred outwards or downwards, depending on the movement direction.

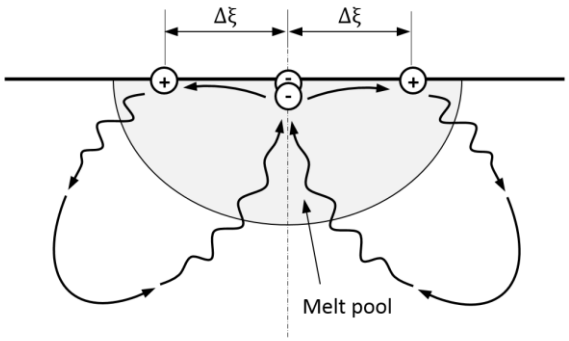

Figure 5: Quadrupole representation of the molten material circulation.

$$T - T_0 = 2P\Delta\xi^2 \left\{ \frac{\left[\frac{V(\xi+\Delta\xi) - V(\xi)}{\Delta\xi}\right] - \left[\frac{V(\xi) - V(\xi-\Delta\xi)}{\Delta\xi}\right]}{\Delta\xi} \right\} \tag{31}$$

When $\Delta\xi$ tends to zero:

$$\mathcal{Q}''_{\xi\xi} = \lim_{\Delta\xi\to 0} 2P(\Delta\xi)^2 \tag{32}$$

$$\mathcal{Q}''_{\eta\eta} = \lim_{\Delta\xi\to 0} 2P(\Delta\eta)^2 \tag{33}$$

$$\mathcal{Q}''_{\zeta\zeta} = \lim_{\Delta\xi\to 0} P(\Delta\eta)^2 \tag{34}$$

Unlike ξ and η directions, in ζ direction there is no need of mirroring the generated material movement. In equation (35), the influence of the material movement in all directions inside the melt pool due to quadrupoles is modelled.

$$T - T_0 = \mathcal{Q}''_{\xi\xi}\left(\frac{\partial^2 V}{\partial\xi^2}\right)_0 + \mathcal{Q}''_{\eta\eta}\left(\frac{\partial^2 V}{\partial\eta^2}\right)_0 + \mathcal{Q}''_{\zeta\zeta}\left(\frac{\partial^2 V}{\partial\zeta^2}\right)_0 \tag{35}$$

$$\left(\frac{\partial^2 V}{\partial\xi^2}\right)_0 = V_0\left[\left(1 + 2\frac{x}{R} + \frac{x^2}{R^2}\right)\left(\frac{v}{2\alpha}\right)^2 + \left(-1 + 2\frac{x}{R} + 3\frac{x^2}{R^2}\right)\left(\frac{v}{2\alpha}\right)\left(\frac{1}{R}\right) + \left(-1 + 3\frac{x^2}{R^2}\right)\left(\frac{1}{R}\right)^2\right] \tag{36}$$

$$\left(\frac{\partial^2 V}{\partial\eta^2}\right)_0 = V_0\left[\left(\frac{y^2}{R^2}\right)\left(\frac{v}{2\alpha}\right)^2 + \left(-1 + 3\frac{y^2}{R^2}\right)\left(\frac{v}{2\alpha}\right)\left(\frac{1}{R}\right) + \left(-1 + 3\frac{y^2}{R^2}\right)\left(\frac{1}{R}\right)^2\right] \tag{37}$$

$$\left(\frac{\partial^2 V}{\partial\zeta^2}\right)_0 = V_0\left[\left(\frac{z^2}{R^2}\right)\left(\frac{v}{2\alpha}\right)^2 + \left(-1 + 3\frac{z^2}{R^2}\right)\left(\frac{v}{2\alpha}\right)\left(\frac{1}{R}\right) + \left(-1 + 3\frac{y^2}{R^2}\right)\left(\frac{1}{R}\right)^2\right] \tag{38}$$

The positive or negative value of the $Q''_{\xi\xi}$, $Q''_{\eta\eta}$ eta $Q''_{\zeta\zeta}$ coefficients has a direct influence on the molten material circulation direction. For instance, a positive value of $Q''_{\xi\xi}$ and $Q''_{\eta\eta}$ implies an outwards material movement in the x and y directions. Moreover, if $Q''_{\zeta\zeta}$ is negative the heat will flow towards the weld crown and the resulting clad will have a wide and shallow geometry. On the contrary, if $Q''_{\xi\xi}$ and $Q''_{\eta\eta}$ present a negative value and $Q''_{\zeta\zeta}$ is positive, narrow and depth clads are obtained. Therefore, their values need to be established according to the welded materials and process parameters.

Consequently, considering the influence of monopoles, dipoles and quadrupoles, the temperature increase generated by a P power heat that moves with a *v* feed rate is determined

by equation (39) where the function G(R) is defined in equation (40). In order to avoid infinite sums and considering that the value of the summations decreases as the number of *n* increases, in each node of the mesh a maximum of *n=5* is considered.

$$T = T_0 + P\left[G(R_0) + \sum_{n=1}^{\infty}\left(G(R_n) + G(R_{n'})\right)\right] \tag{39}$$

$$\begin{aligned} G(R) \approx \frac{1}{2\pi k}\frac{e^{-\frac{v}{2\alpha}(R+x)}}{R}\Bigg\{1 &+ \left(\frac{Q'_{\xi}}{P}\right)\left[\left(1+\frac{x}{R}\right)\frac{v}{2\alpha}+\frac{x}{R^2}\right] \\ &+ \left(\frac{Q''_{\xi\xi}}{P}\right)\left[\left(1+2\frac{x}{R}+\frac{x^2}{R^2}\right)\left(\frac{v}{2\alpha}\right)^2+\left(-1+2\frac{x}{R}+3\frac{x^2}{R^2}\right)\left(\frac{v}{2\alpha}\right)\left(\frac{1}{R}\right)\right. \\ &\left.+\left(-1+3\frac{x^2}{R^2}\right)\left(\frac{1}{R}\right)^2\right] \\ &+ \left(\frac{Q''_{\eta\eta}}{P}\right)\left[\left(\frac{y^2}{R^2}\right)\left(\frac{v}{2\alpha}\right)^2+\left(-1+3\frac{y^2}{R^2}\right)\left(\frac{v}{2\alpha}\right)\left(\frac{1}{R}\right)+\left(-1+3\frac{y^2}{R^2}\right)\left(\frac{1}{R}\right)^2\right] \\ &+ \left(\frac{Q''_{\zeta\zeta}}{P}\right)\left[\left(\frac{z^2}{R^2}\right)\left(\frac{v}{2\alpha}\right)^2+\left(-1+3\frac{z^2}{R^2}\right)\left(\frac{v}{2\alpha}\right)\left(\frac{1}{R}\right)+\left(-1+3\frac{y^2}{R^2}\right)\left(\frac{1}{R}\right)^2\right]\Bigg\} \end{aligned} \tag{40}$$

2.6. Microstructure modelling

The Dendrite Arm Spacing (DAS) is related to the cooling gradient and the limit-temperatures, T_{liq} and *γ/laves* T_e eutectic temperature, respectively. In that temperature range dendrites grow in the favourable crystallographic directions, forming the primary and secondary dendrites [18]. In the present research work, the secondary DAS (SDAS) is modelled, which is calculated using equation (41). The value of the constant *C* depends on the material and for the Inconel 718 has a value of 10 [19].

$$SDAS = C \cdot \left(\frac{T_{liq} - T_e}{\frac{dT}{dt}}\right)^{1/3} \tag{41}$$

SDAS is measured in two different regions in the centre plane of the weld bead, as detailed in Figure 6. The first region, named as R1, is at a 0.2 mm distance from the surface, whereas the second region, named as R2, is at a 1 mm distance from the surface. In each region, 10 measurements are performed, and average values are obtained. Similarly, the cooling rate at the surface of the weld bead is also calculated, region named as R0.

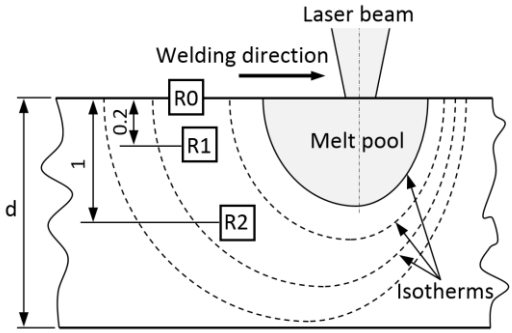

Figure 6: Cross section of the weld bead, where regions 0, 1 and 2 are highlighted.

3. Experimental test

3.1. Employed materials

The material used in the welding tests is the Inconel 718, which is a nickel-based heat resistant superalloy that is widely used in aircraft engines. The welded specimens are 2 mm thick, which is a typical thickness for the welded sheets in components such as the Tail Bearing House (TBH) of the Low-Pressure Turbine (LPT). Composition of this material is detailed in Table 2 [20].

Table 2: Chemical composition of Inconel 718 [20].

Ni	Fe	Cr	Nb	Mo	Ti	Al	Co	Mn	Si	C	Cu	Rest
52.40	18.60	18.60	4.89	3.03	0.98	0.55	0.28	0.24	0.06	0.05	0.05	0.27

Properties of Inconel 718 are detailed in Figure 7. Their values are obtained from literature [21]. Nevertheless, values only until 1873 are found and in the present model, they are extended linearly for higher temperatures until the vaporizing temperature of the Inconel 718, approximately 3100 K. Values from the bibliography are represented with a continuous line, whereas the extended data is plotted by a dashed line.

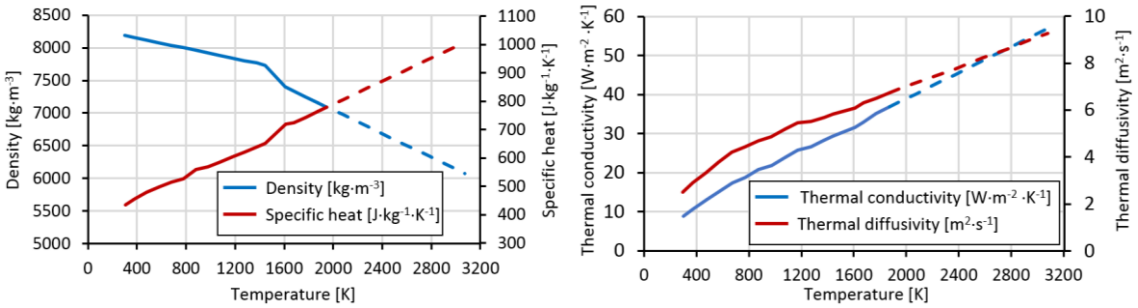

Figure 7: Thermophysical properties of the Inconel 718 alloy [21].

Similarly, knowing that the absorptivity of Inconel 718 is 0.3 at room temperature and that the keyhole works as a black body [9], absorptivity is defined to vary linearly until a unit value is reached at the nickel vaporizing temperature.

For determining the SDAS developed during the solidification of the welded Inconel 718, the temperature values proposed by Einselstein are considered [22], which are detailed in Table 3.

Table 3: Reaction temperatures of Inconel 718 [22].

Reaction stages in cooling	Temperature [°C]
Liquidus	1260
Υ/laves eutectic	1177

3.2. Used equipment

A Rofin FL010 fibber laser with a 1 kW maximum output power and a 0.1 mm spot size is employed for the experimental test. Besides, a galvanometric scanner, model hurryScan 25, is used to perform the superposed oscillation movement of the laser beam during the welding process. Both individual movements are depicted in Figure 1, as well as the resultant combination. A 5-axis Cartesian machine controls the position of the scanner, which comprises the slow axes, whereas the scanner is controlled by means of the software VLM.

A clamping device is used to minimize the existing gap between the faces of the plates and avoid misalignments of the plates during the welding tests, due to the thermal stresses. Argon 2X is used as a protective gas in all the tests. Besides, a specific setup to generate the protective atmosphere in the upper and lower faces of the weld and avoid oxidation of the material is manufactured. The device, which is shown in Figure 8 consists of four pipes, two in the upper face and two in the lower face, each one with an opening where the argon exits and is directed towards the welding region. This way, total protection of the weld bead is achieved both in the crown and in the root.

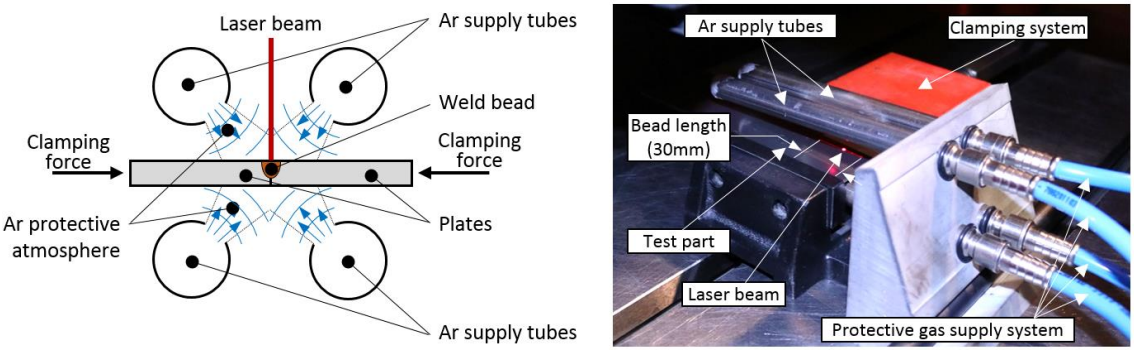

Figure 8: Employed setup for the experimental tests.

3.3. Tests carried out

In Table 4 all test carried out are detailed. In all tests, a constant total 24 l·min^{-1} argon gas flow is used, and the laser beam is focused at the upper face of the plates

Table 4: Test carried out and the employed process conditions.

Test	P [W]	v_f [m·s^{-1}]	v_p [m·s^{-1}]	d_w [mm]
1	350	3	84.8	0.9
2	400	3	84.8	0.9
3	450	3	84.8	0.9
4	500	3	84.8	0.9
5	350	5	197.9	0.9
6	400	5	141.4	0.9
7	450	5	141.4	0.9
8	500	5	141.4	0.9
9	450	7	197.9	0.9
10	500	7	197.9	0.9
11	550	7	197.9	0.9
12	600	7	197.9	0.9
13	350	3	179.1	1.9
14	400	3	179.1	1.9
15	450	3	179.1	1.9
16	500	3	179.1	1.9
17	350	5	298.5	1.9
18	400	5	298.5	1.9
19	450	5	298.5	1.9
20	500	5	298.5	1.9

During the tests, the temperature at the centre of the clad is measured using a two-colour Igar 12-LO pyrometer. The pyrometer is installed in a fix position, which enables to measure the heating and cooling cycles of the material as the laser passes by. The pyrometer extracts a measurement every 8 milliseconds.

3.4. Specimen analysis procedure

After the welding tests are performed, weld beads are cut and cross sections are encapsulated using a phenolic resign. Afterward, specimens are polished until a mirror surface is achieved and etched using Marble reactive for 10 seconds. This reactive reveals the microstructure as well as enables to differentiate the melted and heat affected regions from the rest of the plates not affected by the welding process.

Two microscopes are used for analysing the welded cross sections. On the one hand, a Leica Z6 APO coupled with a Leica DFC 295 colour camera is used to obtain macro pictures and measure their geometrical features, uncertainty of the equipment is a magnitude order below the measured magnitudes. On the other hand, a Nikon OPTIPHOT 100 microscope is used for analysing the microstructure in different regions of the clad.

4. Model validation

For the validation of the model, geometries of the weld beads and developed temperatures on the surface have been considered. Besides, the resulting microstructure is evaluated on the experimental cross sections and compared with the values predicted by the model

4.1. Geometry comparison

4.1.1. Time and area factor determination

The width of the clads is determined based on Carslaw-Jaeger model. For that purpose, the area and time factors need to be calculated. Values of both factors are shown in Table 5. The area factor is obtained using equation (13), whereas the time factor is obtained empirically in order to minimize the simulation error. Afterward, this second factor is related to the employed process parameters.

Table 5: Employed area and time factors.

Test	S_{factor} [-]	t_{factor} [-]
1,2,3,4	2.778	2.000
5,6,7,8	2.778	2.285
9,10,11,12	2.778	2.394
13,14,15,16	5.263	2.100
17,18,19,20	5.263	2.863

It is concluded that the time factor is independent of the employed laser power and depends mainly on the wobble diameter (d_w), the feed rate (v_f) and the peripheral velocity of the wobble (v_p). In order to extrapolate the developed model to different situations and process parameters from those studied in the present case, in Figure 9 the time factor is approximated by means of linear regression, with an R^2 of 0.9522. In equation (42), the coefficients m and b take the values of $4 \cdot 10^{-4}$ and 1.89, respectively.

$$t_{factor} = m \cdot d_w \cdot v \cdot v_p \cdot e^{-3 \cdot \left(\frac{S_h \cdot t_{in}}{S_f}\right)} + b \tag{42}$$

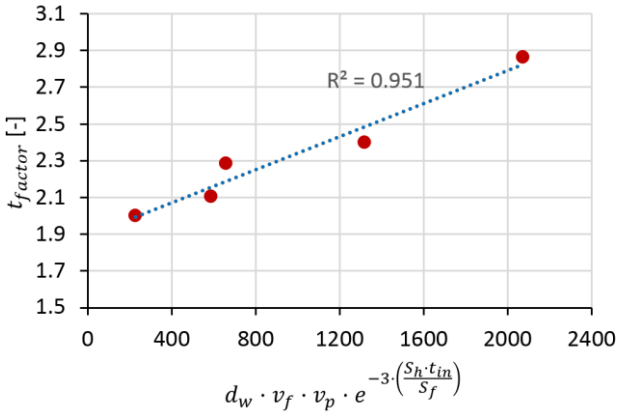

Figure 9: Empirically defined time factor for different process parameters (red dots) and the linear approximation.

4.1.2. Weld width

In Table 6 the comparison between the experimentally measured width and the value predicted by the model is presented. As can be seen, an error below 0.05 mm is obtained between the model and the experimentally measured width.

Table 6: Weld bead width results

Test	Real width [mm]	Sim width [mm]	Error [mm]
1	1.78	1.78	0.00
2	1.96	1.94	0.02
3	2.09	2.09	0.00
4	2.18	2.18	0.00
5	1.61	1.62	-0.01
6	1.77	1.78	-0.01
7	1.90	1.88	0.02
8	1.97	1.98	-0.01
9	1.70	1.70	0.00
10	1.77	1.76	0.01
11	1.83	1.82	0.01
12	1.94	1.94	0.00
13	2.44	2.42	0.02
14	2.69	2.66	0.03
15	2.86	2.82	0.04
16	3.05	3.02	0.03
17	2.22	2.24	-0.02
18	2.28	2.30	-0.02
19	2.47	2.48	-0.01
20	2.59	2.60	-0.01

In Figure 10 the isotherms of the weld bead are shown once a stable regime is obtained. The red line represents the limit of the melt pool generated by the laser beam and corresponds to the solidus temperature, which is 1,533K for the Inconel 718.

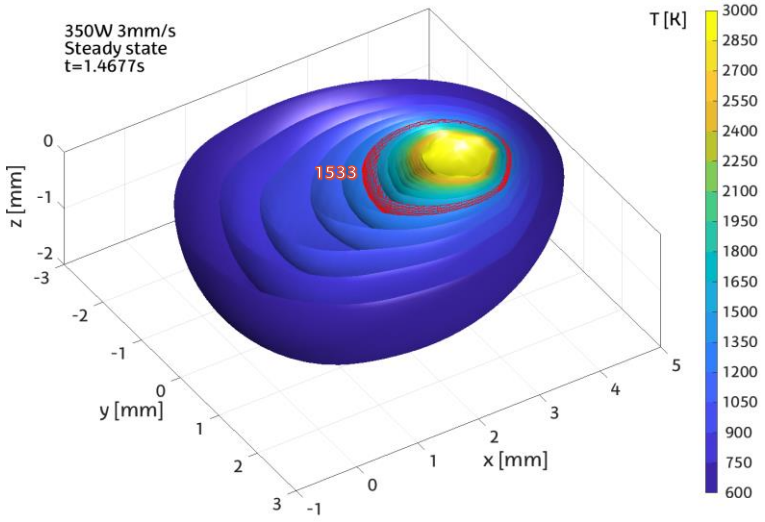

Figure 10: Isotherms of the weld bead corresponding to test 1, once a stable regime is achieved.

In following Figure 11 the longitudinal and transversal cross-sections of the weld bead shown in Figure 10 are shown, sections corresponding to test 1. As can be seen, the model can predict the asymmetry typical of the welding process and the wake that appears in the rear of the melt pool.

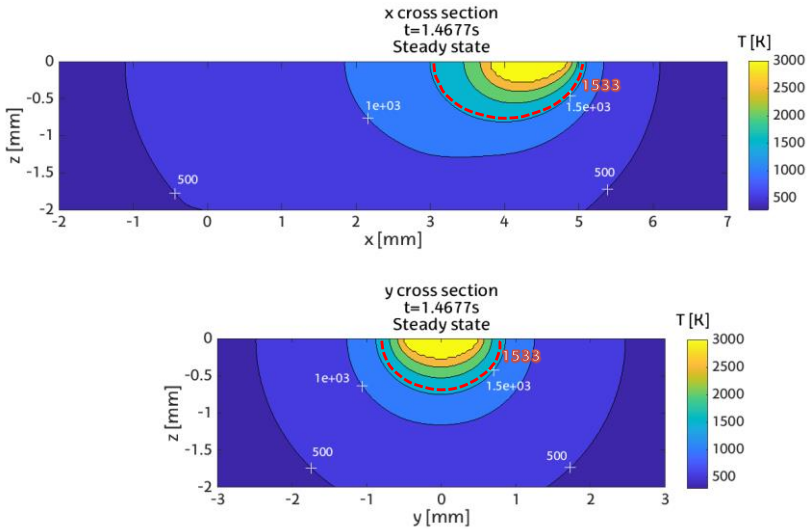

Figure 11: Longitudinal and cross sections of the weld bead corresponding to test 1, once the welding process is stabilized.

4.1.3. Weld depth

Prior to obtaining the modelled values of the weld depth, the values of the parameters $Q''_{\xi\xi}$, $Q''_{\eta\eta}$ eta $Q''_{\zeta\zeta}$ need to be experimentally determined for the Inconel 718: $Q'_{\xi} = -\left(t_{factor} \cdot 10^{-3}\right)$, $Q''_{\xi\xi} = Q''_{\eta\eta} = -\left(t_{factor} \cdot 10^{-6}\right)$ and $Q''_{\zeta\zeta} = \left[\left(t_{factor}\right)^2 \cdot D \cdot 10^{-6}\right]$. In Table 7 a comparison between the real and modelled values is shown.

Table 7: Weld depth results

Test	Real depth [mm]	Sim depth [mm]	Error [mm]
1	1.51	1.40	0.11
2	2.00	2.00	0.00
3	2.00	2.00	0.00
4	2.00	2.00	0.00
5	0.92	1.18	-0.27
6	1.21	1.36	-0.15
7	1.56	1.42	0.14
8	2.00	2.00	0.00
9	1.28	1.28	0.00
10	1.32	1.36	-0.04
11	1.71	1.44	0.27
12	2.00	2.00	0.00
13	0.72	1.00	-0.28
14	1.27	1.24	0.03
15	1.57	1.28	0.29
16	2.00	2.00	0.00
17	0.40	0.66	-0.26
18	0.56	0.78	-0.22
19	0.77	1.02	-0.25
20	0.88	1.16	-0.28

Obtained error is below 300 µm, which ensures the accuracy of the model for different welding conditions. In Figure 12 the longitudinal and cross-section of the weld bead corresponding to test 1 are shown, as well as a comparison between the modelled and real cross sections.

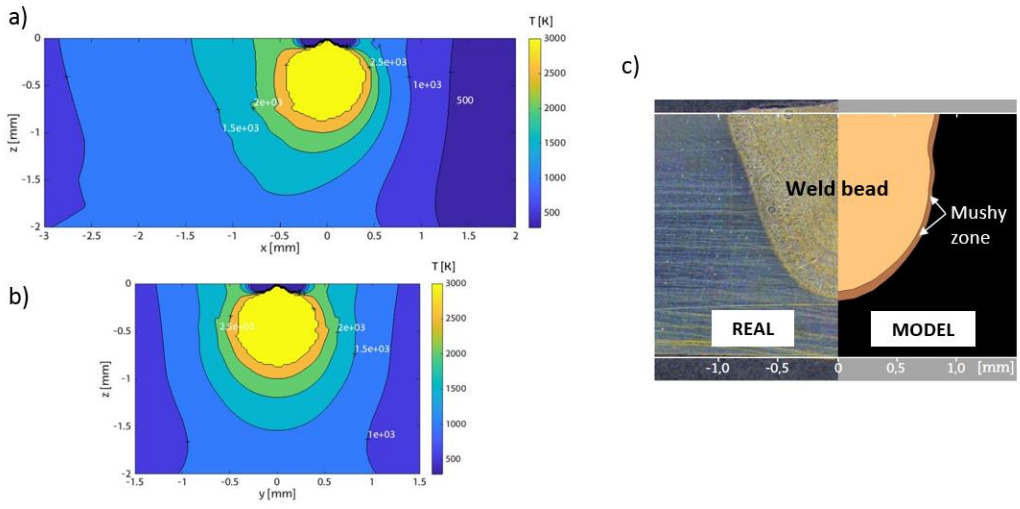

Figure 12: a) Longitudinal and b) ross sections of the weld bead corresponding to test 1, once the welding process is stabilized. c) Real and model cross section comparison for test 1.

4.2. Temperatures and microstructure comparison

Besides the capability of the model to predict the shape of the weld bead, the model is able to predict the thermal field variations on the welded plates and the resulting microstructure. Temperature evolution on the surface is measured directly by using a two-colour pyrometer, whereas the inner temperature variations are studied based on the developed microstructure once the part is cooled down.

4.2.1. Surface cooling gradient measurement

The temperature is measured in the centre of the weld bead; region named as R0. The signals obtained from the two-colour pyrometer are filtered in Matlab in order to ease their analysis and avoid oscillations. Resulting data is shown in Figure 13.

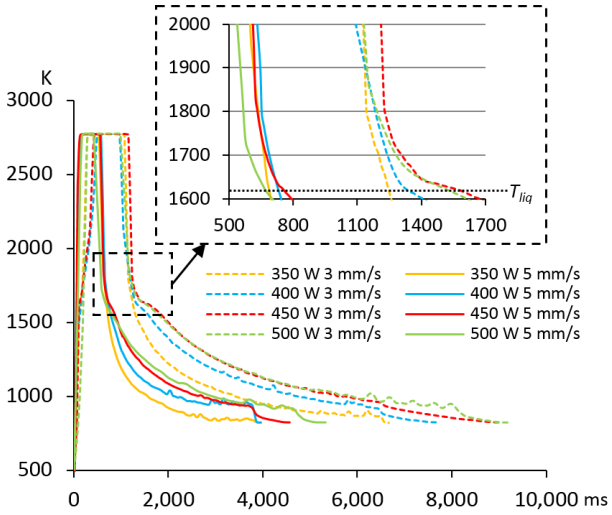

Figure 13: Temperature measurements for different tests when a 1 mm wobble diameter is used.

Afterward, the cooling rate is calculated by means of measuring the amount of time required for lowering the temperature of the weld bead from slightly above the liquidus temperature until the solidus temperature. Obtained values, together with the process parameters in order to ease their understanding, are compared with those predicted by the model and error values are shown in Table 8.

Table 8: Cooling rates at the surface, in the centre of the weld bead.

Test number	P [W]	v_f [mm·s^{-1}]	Cooling rate [K·s^{-1}]		Error [K·s^{-1}]	Error %
			Experimental	Model		
1	350	3	2459	159	159	6.5
2	400	3	1860	-96	-96	-5.2
3	450	3	1587	53	53	3.3
4	500	3	1025	82	82	8.0
5	350	5	6030	-220	-220	-3.6
6	400	5	4929	-154	-154	-3.1
7	450	5	4435	-273	-273	-6.2
8	500	5	1932	99	99	5.1

4.2.2. SDAS measurement

Weld beads are cross sectioned and etched in order to reveal the microstructure in regions R1 and R2, Figure 14. In each test part 10 individual measurements are performed in each region for obtaining the average SDAS.

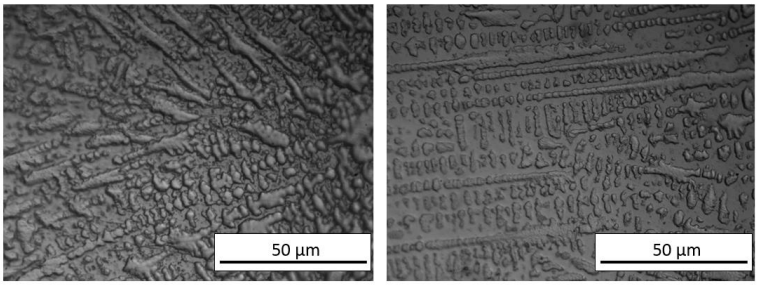

Figure 14: Microstructure of test 1 in regions R1 (left) and R2 (right).

In parallel, analysing the model results, the cooling gradient is calculated in both regions, R1 and R2, by means of the amount of time required to cool down from the liquidus (1609 K) to the solidus temperature (1533 K). Afterward, equation (41) is applied and the SDAS value corresponding to the calculated cooling rate is obtained, see Table 9.

Table 9: Average SDAS values measured at different regions.

Test number	R1		R2	
	Cooling rate [K·s^{-1}]	**SDAS [µm]**	**Cooling rate [K·s^{-1}]**	**SDAS [µm]**
1	2400	4.046	2600	3.940
2	1933	4.349	1909	4.367
3	1627	4.606	1500	4.733
4	1111	5.231	1217	5.075
5	7000	2.832	6625	2.884
6	5333	3.101	5917	2.995
7	4375	3.312	4750	3.223
8	3708	3.500	3875	3.449

In order to reduce the number of analysed samples, the weld beads corresponding to the limit welding parameters are studied. The error of the model when predicting the SDAS is detailed in Table 10, where results corresponding to both R1 and R2 regions are shown. In all cases, an error below 1 µm is obtained.

Table 10: Experimental and modelled SDAS values comparison

Test number	R1				R2			
	Experimental	**Model**		Error [µm]	**Experimental**	**Model**		Error [µm]
	Average SDAS [µm]	Cooling rate [K·s^{-1}]	SDAS [µm]		Average SDAS [µm]	Cooling rate [K·s^{-1}]	SDAS [µm]	
1	3.701	2400	4.046	0.345	3.185	2600	3.940	0.755
4	4.249	1111	5.231	0.249	3.775	1217	5.075	-0.169
5	2.583	7000	2.832	0.982	3.053	6625	2.884	0.881
8	2.626	3708	3.500	0.874	3.537	3875	3.449	-0.088

5. Conclusions

In the present work, an analytic model for LBW based on the classical heat transfer equations is developed and validated. To that end, an experimental setup is developed, and various tests are performed in order to evaluate the model under different conditions. According to the obtained results, the following conclusions can be drawn:

- Thanks to a double analytical model, both the weld bead width and depth are accurately modelled. Besides, by introducing the effect of monopoles, dipoles and quadrupoles, the model can consider the effect of molten material movement inside the weld bead at a low computational cost.
- It is verified that the surface and time factors introduced in the model in order to simulate the wobble strategy enhance the accuracy of the model. Errors below 0.05 mm and 0.3 mm are obtained regarding the clad width and depth, respectively.
- The error in the surface cooling rate is below 300 $K \cdot s^{-1}$. On the one hand, this error is attributed to the fast nature of the welding process, which makes difficult to model this parameter precisely. On the other hand, an approximation of the laser heat source is employed, which introduces an inherent error in the model. Nevertheless, this accuracy is adequate considering the low computational cost of an analytical model.
- The model results to predict the SDAS with an error below 1 µm. Besides, the model shows the same behaviour as the experimental results, where an increase of the laser power results in a lower cooling rate and higher SDAS, and an inverse situation is encountered when the laser feed rate is raised.

Acknowledgements

Authors gratefully acknowledge the University of the Basque Country (UPV/EHU) for its financial help. In addition, this work has been carried out in the framework of the "*Entorno Virtual de Diseño y Fabricación de Turbinas Aeronáuticas*" ENVIDIA project (RTC-2017-6150-4) funded by the Spanish Ministry of Industry and Competitiveness.

References

[1] M.S. Węglowski, S. Błacha, A. Phillips, Electron beam welding - Techniques and trends - Review, Vacuum. 130 (2016) 72–92. doi:10.1016/j.vacuum.2016.05.004.

[2] J. Blackburn, Laser welding of metals for aerospace and other applications, in: Weld. Join. Aerosp. Mater., Woodhead Publishing, 2011: pp. 75–108. doi:10.1016/B978-1-84569-532-3.50003-4.

[3] John Michael Dowden, The Theory of Laser Materials Processing. Heat and Mass Transfer in Modern Technology, Chapman and Hall/CRC, 2017. doi:https://doi.org/10.1007/978-3-319-56711-2.

[4] S.. Tsirkas, P. Papanikos, T. Kermanidis, Numerical simulation of the laser welding process in butt-joint specimens, J. Mater. Process. Technol. 134 (2003) 59–69. doi:10.1016/S0924-0136(02)00921-4.

[5] W. Spraragen, G.E. Claussen, Temperature distribution during welding - A review of the literature to January 1, 1937, Weld. J. Res. Sup. 16 (1937) 4–10.

[6] D. Rosenthal, Theoretical Study of the Heat Cycle During Arc Welding, in: 2eme Congr.

Natl. Des Sci. Brussels, 1935: p. 1277.

[7] D. Rosenthal, Mathematical theory of heat distribution during welding and cutting, Weld. J. 20 (1941) 220–234.

[8] H.S. Carslaw, J.C. Jaeger, Conduction of heat in solids, 2nd ed., Oxford: Clarendon Press, 1959.

[9] J. Mazumder, Laser Welding, in: Mater. Process. Theory Pract., Elsevier, 1983: pp. 113–200. doi:10.1016/B978-0-444-86396-6.50009-X.

[10] J. Goldak, A. Chakravarti, M. Bibby, A new finite element model for welding heat sources, Metall. Trans. B. 15 (1984) 299–305. https://link.springer.com/content/pdf/10.1007/BF02667333.pdf.

[11] M. Kubiak, W. Piekarska, Z. Saternus, T. Domański, Numerical Prediction of Fusion Zone and Heat Affected Zone in Hybrid Yb:YAG laser + GMAW Welding Process with Experimental Verification, Procedia Eng. 136 (2016) 88–94. doi:10.1016/J.PROENG.2016.01.179.

[12] K. Kazemi, J.A. Goldak, Numerical simulation of laser full penetration welding, Comput. Mater. Sci. 44 (2009) 841–849. doi:10.1016/J.COMMATSCI.2008.01.002.

[13] H. Zhao, W. Niu, B. Zhang, Y. Lei, M. Kodama, T. Ishide, Modelling of keyhole dynamics and porosity formation considering the adaptive keyhole shape and three-phase coupling during deep-penetration laser welding, J. Phys. D. Appl. Phys. 44 (2011) 485302. doi:10.1088/0022-3727/44/48/485302.

[14] L.J. Zhang, J.X. Zhang, A. Gumenyuk, M. Rethmeier, S.J. Na, Numerical simulation of full penetration laser welding of thick steel plate with high power high brightness laser, J. Mater. Process. Technol. 214 (2014) 1710–1720. doi:10.1016/J.JMATPROTEC.2014.03.016.

[15] D. Rosenthal, The Theory of Moving Sources of Heat and Its Application to Metal Treatments, Trans. ASME. 68 (1946) 849–866.

[16] A.C. Nunes, An extended Rosenthal weld model, Weld. J. 62 (1983) 165–170.

[17] K.C. Mills, B.J. Keene, R.F. Brooks, A. Shirali, Marangoni effects in welding, in: Philos. Trans. R. Soc. London. Ser. A Math. Phys. Eng. Sci., 1998: pp. 911–925.

[18] G.D. Janaki Ram, A. Venugopal Reddy, K. Prasad Rao, G.M. Reddy, J.K. Sarin Sundar, Microstructure and tensile properties of Inconel 718 pulsed Nd-YAG laser welds, J. Mater. Process. Technol. 167 (2005) 73–82. doi:10.1016/J.JMATPROTEC.2004.09.081.

[19] A.D. Patel, Y.V. Murty, Effect of Cooling Rate on Microstructural Development in Alloy 718, in: Superalloys 718, 625, 706 Var. Deriv. TMS (The Miner. Met. Mater. Soc., 2001: pp. 123–132.

[20] H. International, Haynes International, (n.d.). https://www.haynesintl.com/alloys/alloy-portfolio_/High-temperature-Alloys/haynes718-alloy/principal-features.aspx.

[21] K.C. Mills, Ni - IN 718, in: K.C. Mills (Ed.), Recomm. Values Thermophys. Prop. Sel. Commer. Alloy., Woodhead Publishing, 2002: pp. 181–190. doi:doi.org/10.1533/9781845690144.181.

[22] T. Antonsson, H. Fredriksson, The effect of cooling rate on the solidification of INCONEL 718, Metall. Mater. Trans. B. 36 (2005) 85–96. doi:10.1007/s11663-005-0009-0.